Applied Surface Science 606 (2022) 154770

Contents lists available at ScienceDirect

Applied Surface Science

journal homepage: www.elsevier.com/locate/apsusc

Full length article

Scanning-resonance optical sensing based on a laterally graded plasmonic layer—optical properties of Ag_xAl_{1-x} in the range of $x = 0$ to 1

Benjamin Kalas [a,b], György Sáfrán [a], Miklós Serényi [a], Miklós Fried [a,c], Péter Petrik [a,d,*]

[a] Institute for Technical Physics and Materials Science, Centre for Energy Research, Konkoly-Thege Rd. 29-33, 1121 Budapest, Hungary
[b] Doctoral School of Physics, Faculty of Science, University of Pécs, 7624 Pécs, Ifjúság útja 6, Pécs, Hungary
[c] Institute of Microelectronics and Technology, Óbuda University, Tavaszmezo u. 17, 1084 Budapest, Hungary
[d] Department of Electrical and Electronic Engineering, Institute of Physics, Faculty of Science and Technology,University of Debrecen, 4032 Debrecen, Hungary

ARTICLE INFO

Keywords:
Combinatorial material science
Spectroscopic ellipsometry
Plasmonics
Biosensing

ABSTRACT

Plasmonic $AgAl/Si_3N_4$ sensor layer structure was deposited on a fused silica glass slide by dual DC magnetron sputtering. The composition of the Ag_xAl_{1-x} layer was laterally graded in which x linearly changes from $x = 0$ to $x = 1$ over a distance of 20 mm. The Si_3N_4 layer serves both as a resonator and a protective layer providing homogeneous chemical properties on top of the inhomogeneous AgAl layer. The structure was illuminated through a hemi-cylinder for variable-angle measurements in the Kretschmann–Raether configuration using a focused spot that enabled the change of x by moving it along the gradient of the composition. Optical properties of Ag_xAl_{1-x} in the whole composition range were obtained. The positions of resonant peaks were shifted by changing the angle of incidence and the lateral position of the spot in a flow-cell configuration. The optical sensing performance of the bilayer system was investigated for x=0 and x=1. Based on the capabilities of ellipsometry limit of detection in refractive index unit values of $\approx 4 - 8 \cdot 10^{-6}$ can be achieved in the resonant positions utilizing both p- and s-polarizations. Due to the flexible tunability of the resonant wavelengths by moving a focused spot, the above sensitivity is available in-situ, over the spectral range of 265-1504 nm.

1. Introduction

Plasmonics is the field of research and technology that introduces the interactions between the electric field component of incident light and free electrons in metallic thin films or various metallic nanostructures [1]. At the interface of metal layers and dielectrics (e.g. air or liquids), plasmons interacting with light result in a surface plasmon polariton (SPP) resonance: originating from a strongly confined surface wave that propagates along the interface and decays exponentially in both the metal film and the dielectric ambient.

An effective method for tuning the optical response of metallic thin films and nanostructures, i.e., to subtly customize the optimum wavelength range for SPP, the chemical composition of the plasmonic material is modified by alloying various metals [2–6]. Originally, for SPP applications noble metals such as Ag, Au and Pt have been the preferred choice owing to their abundant free electrons despite the well-known optical losses introduced by interband optical transitions [7–9]. In the past few years, however, earth-abundant metals, such as Al and Mg, have also been used as a new class of materials for low-optical-loss and low-cost optical components [10]. For on-chip nanophotonics applications, metals like Al and Cu are ideal choices since their fully complementary metal–oxide–semiconductor (CMOS) compatibility along with their abundance on earth result in low-cost device processing [6]. Furthermore, pertaining to the large free electron densities observed in metal alloys and intermetallics, they are also promising choices as alternative plasmonic materials [7].

Alloying of metals via physical deposition methods lead to almost arbitrary tunability regarding their optical behavior in the ultraviolet–visible–near infrared (UV–Vis–NIR) wavelength range. This flexible control of the spectrum has also enabled the further development of a variety of advanced optoelectronic devices, such as switches [11] and biosensors [12]. It has been shown earlier that alloying Ag or Au with another metal that contributes two or three electrons per atom to the free electron gas can significantly modify the reflection and absorption spectra [13].

As an example the investigation of single-phase Ag–Cu with different composition has led to the conclusion that the optical properties of these alloys could be efficiently manipulated by the annealing temperature and the composition thus making Ag–Cu an attractive material

* Corresponding author at: Institute for Technical Physics and Materials Science, Centre for Energy Research, Konkoly-Thege Rd. 29-33, 1121 Budapest, Hungary.
E-mail address: petrik.peter@ek-cer.hu (P. Petrik).

https://doi.org/10.1016/j.apsusc.2022.154770
Received 23 April 2022; Received in revised form 16 August 2022; Accepted 31 August 2022
Available online 12 September 2022

for plasmonics [14]. The dielectric properties of a number of alloy systems, such as Au-Ag [3,15], Ag–Cu [3,14] and Au-Cu [3] have been examined using optical spectroscopy, and a combinatorial gold–aluminium (Au_xAl_{1-x}) layer has also been introduced previously [16]. Several examples for alloys with possible use in the field of plasmonics have also been presented in Ref. [17].

Ag is routinely used in various applications due to its excellent optical and electrical characteristics. Ag has the most favorable properties for plasmonic applications of any material in the Vis–NIR range [17], and is widely available. However, the thickness and surface roughness of an Ag layer can significantly influence these advantageous properties [18], inducing unfavorable deviations compared to an ideal Ag layer. The island formation during thin Ag film growth [19] ultimately leads to a rough and semicontinuous layer with additional optical loss due to excitation of plasmon resonances [20]. It is known that Ag follows the Volmer–Weber growth model [21] in which the deposited Ag atoms initially form isolated islands. As the deposition continues, these islands grow further and eventually connect to form a semicontinuous layer. To overcome this problem, a 1–2 nm thin germanium (Ge) layer can be deposited under the Ag layer [22,23]. This method has led to a reduced surface roughness value and a decreased percolation threshold for Ag nanofilms (the latter being 10–20 nm typically without the additional Ge layer [24]). However, Ge has high absorption in the visible wavelength range which subsequently leads to a reduced transmittance. To address this situation the deposition of an ultra thin and smooth Ag film has been reported previously [25], which shows both low optical loss and low electrical resistance. This film has been made by involving the co-deposition of only a small amount of Al during Ag deposition without any wetting layer. In the same study it has been found that the incorporation of a small amount of Al suppressed the 3D island growth of Ag and resulted in the formation of an ultra thin layer with a reduced surface roughness of 1 nm and also a reduced percolation threshold of 6 nm. As a promising application, ion-implanted Al–Ag bimetallic substrate has been proposed as an excellent tool for surface enhanced fluorescence (SEF) measurement [26].

Al layer with a high reflectivity throughout the Vis spectral range has been used in optical reflector applications [27]. An Al–Ag alloy-film is also a highly reflective coating which can be used for solar reflectors [28]. The effect of Al on the optical properties of Ag has also been investigated in a 500-nm layer deposited on silicon surface [29]. In the same work a slight blue-shift of the bulk plasma frequency has been observed with increasing Al ratio. It has also been shown that a 7-nm Al-doped Ag film remains stable under ambient conditions for over six months without any protective layer [30]. Al-doped Ag offers additional benefits when compared to pure Ag, such as ultrathin film formation, enhanced thermal and long-term stability, better adhesion with substrates, and improved 3D nanostructure coverage [30,31]. In addition, its optical loss can be further reduced by a simple annealing treatment. It has also been shown that the central position of the interband transition around 1.5 eV is tunable with variable annealing temperatures and different Ag concentrations in Al–Ag alloys [32, 33]. All these merits facilitate the fabrication of high-performance Al plasmonic structures [34,35] along with long range surface plasmon polariton (LR-SPP) waveguides [30].

In this paper, we introduce a thin and smooth combinatorial Ag_xAl_{1-x} alloy film with x including the whole composition range $0 \leq x \leq 1$ deposited by dual DC magnetron sputtering using a scaled-up device [36]. The optical properties of the deposited Ag_xAl_{1-x} alloy film were characterized by variable angle spectroscopic ellipsometry (VASE) in a wide wavelength (λ) range. The intermetallic layer was realized on a fused silica (FS) substrate and it was subsequently covered with a radio-frequency (RF) sputtered Si_3N_4 layer. This additional layer serves dual purposes acting as a protecting layer preventing the interaction between the metal layer/air interface and as a waveguide layer to realize a coupled plasmon-waveguide resonator (CPWR) structure [37–40] in the Kretschmann–Raether (KR) configuration [41]. In this study, the emerging resonance peaks were investigated both theoretically and experimentally. Based on the calculations it was predicted that it is possible to precisely measure the refractive index change of liquids from ultraviolet wavelengths (ca. 260 nm) up to the NIR range (ca. 1500 nm) by using a single compositionally graded sample.

To our knowledge this is the first time that both the lateral thickness and the composition change was manipulated in a controlled way in a combinatorial thin film. It is also the first time that such a structure is used in a sensor structure the properties of which can be varied by laterally moving a focused spot over the interface in a KR configuration. More specifically, we show that not only the composition of the intermetallic layer but also its thickness can be controlled in the range of 15 nm (Al-side) to 40 nm (Ag-side) for realizing a tunable plasmonic sensor structure. By moving the spot and changing the angle of incidence (AOI) this is the first time that a "scanning resonance" tool is realized in which the wavelength position of sensitivity maxima can be scanned and adjusted during the in-situ measurement, resulting in a quantitative "high-sensitivity" spectroscopy method. Our result can also be considered as a proof of concept, based on which a family of sophisticated plasmonic sensors can be built with modulation capabilities

2. Materials and methods

2.1. Deposition of the combinatorial sensor structure

Combinatorial Ag_xAl_{1-x} alloy film was deposited on a 25 mm × 10 mm (width × length) and 150 ± 25 μm thin UV-grade FS substrate (purchased from Valley Design Corp) by "single-sample" micro-combinatory at room temperature. The deposition resulted in a layer with gradient composition of Ag_xAl_{1-x} with x ranging in $0 \leq x \leq 1$. The 25 mm long substrate exhibits a 20 mm long gradient Ag_xAl_{1-x} track enclosed between 2.5 mm long lead-in sections of one target's flux.

A stainless steel UHV system by dual DC magnetron sputtering was used which is a scaled-up device [36] originally developed for synthesizing micro-combinatorial transmission electron microscopy samples. The present arrangement sweeps a shutter with a 1 mm × 10 mm slot in fine steps above the substrate meanwhile the power of the two magnetron sources is regulated in sync with the slot movement (Fig. 1). As the slot passes over the substrate, the fluence of Ag gradually decreases from 100% to 0%, while that of Al increases from 0% to 100%, which creates the required gradient of the composition. The maximum values of the applied power for the Ag and Al targets were 150 W and 330 W, respectively. The variable thickness was also achieved by the fine regulation of the slot movement. The capability of "single-sample" micro-combinatory has been demonstrated for amorphous Si_xGe_{1-x} thin layers recently [42,43]. In these works, excellent composition linearity has been found along the sample position.

The main advantages of the combinatorial deposition technique are the following: (i) The deposited layer is prepared in one process step which assures that all the parameters of the sample preparation and also the substrate properties are the same—except for the modulated parameter (the composition and/or thickness). (ii) The optical measurement and the evaluation are also easier and more efficient, since they can automatically be performed by a lateral scan over the sample surface. The evaluation process also supports a single-process interpretation. (iii) The combinatorial technique also allows the characterization of larger modulations and unexpected variations of the properties without any assumption of the lateral dependence.

The deposition of the Si_3N_4 cover layer was realized by RF sputtering, the variable thickness (from 180 nm to 250 nm) of this layer was achieved by the careful regulation of the linear movement of a cover-plate over the sample. To minimize the disadvantageous effect of air on the metallic combinatorial layer, RF sputtering was applied immediately after the Ag_xAl_{1-x} alloy film deposition.

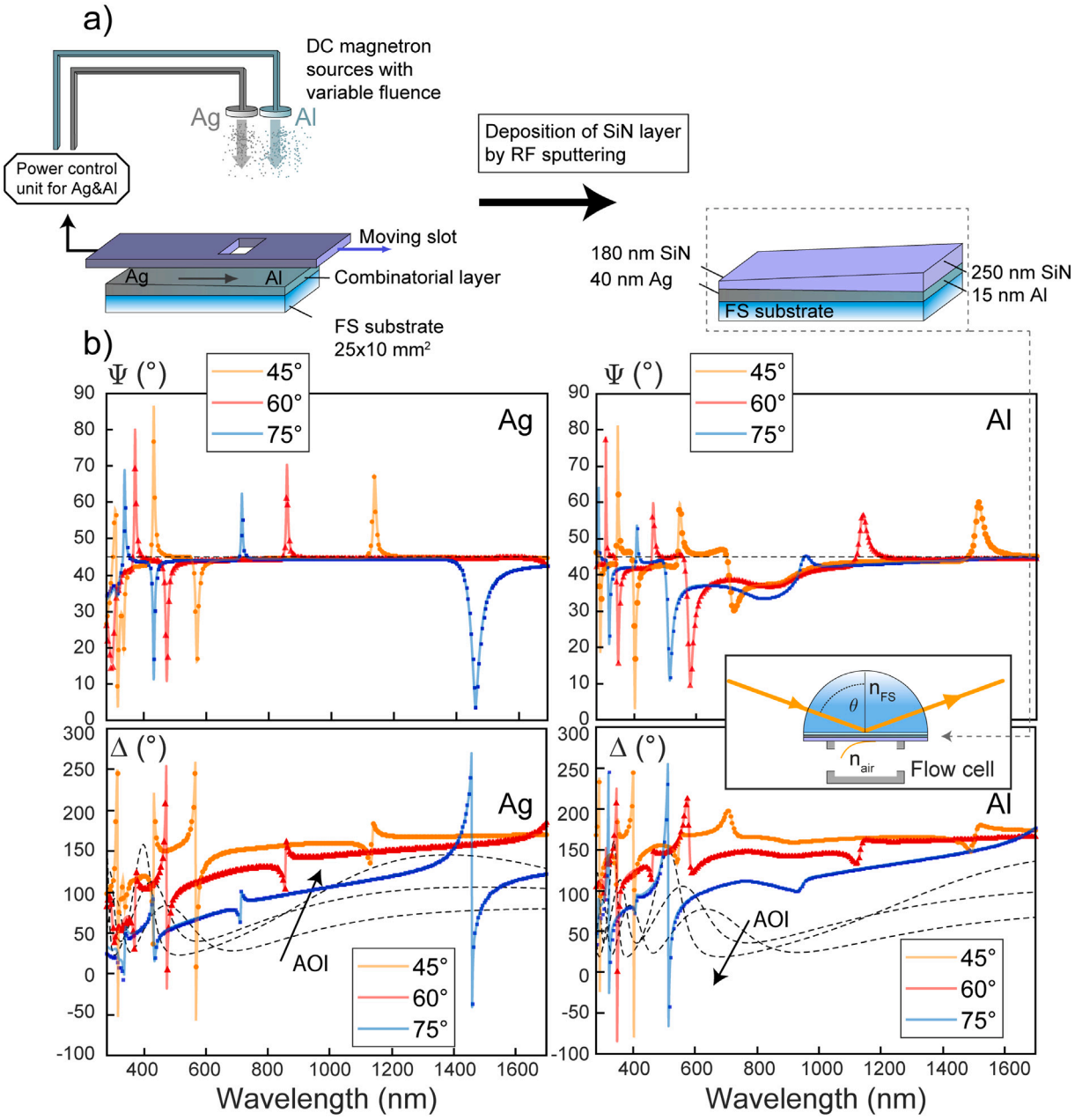

Fig. 1. (a) Deposition of the combinatorial Ag_xAl_{1-x} layer and Si_3N_4 layer on the top of it. (b) Simulated spectra with x = 0,1 (pure Al and Ag, respectively) at different AOIs in the KR-configuration (inset figure). Solid lines show TMM simulated results, while discrete points show FEM calculations. Black dashed curves depict the spectra for a structure without the combinatorial AgAl layer (i.e., only Si_3N_4 layer is present with thickness values of 180 nm and 250 nm, respectively). Arrows point toward increasing AOI values of the black dashed lines.

2.2. Simulated optical spectra

In order to achieve the best sensitivity in the KR-configuration, optical simulations were carried out to optimize the thicknesses of both the Ag_xAl_{1-x} (at $x = 0, 1$) alloy film and the Si_3N_4 film prior to the layer deposition. These simulations were implemented using the transfer matrix (TMM) and finite element (FEM) methods. The TMM calculations were conducted via the commercial software CompleteEASE, and the FEM calculations were carried out using COMSOL Multiphysics. For both implementations, the optical spectra were calculated in the λ-range of 250 nm–1690 nm and AOIs (θ) of 45°–75°. The dielectric functions $\varepsilon = \varepsilon_1 - i\varepsilon_2$ $[= N^2 = (n - ik)^2]$ of Ag and Al were imported from Ref. [44].

The optimized thicknesses were carefully chosen to fulfill all the advantages of the layer system: (i) realization of multiple resonance peaks in the wavelength spectra at a single AOI, (ii) emergence of resonance peaks of both p- and s-polarizations and also (iii) the possible realization of narrower resonance peaks (compared to a single metallic layer) is also possible. (iv) The solely changing parameter along the sample is the chemical composition of the Ag_xAl_{1-x} layer. The properties of the Si_3N_4-liquid interface remain the same, thus the adsorption of biological molecules would not be influenced by the different composition. Si_3N_4 is a widely used material due to its excellent thermal and chemical stability with a large bandgap of ≈5 eV [45,46], also being used for biosensor applications [47].

The optimal thickness value of the Ag layer was fixed at 40 nm (the reported optimal thickness for Au in most research papers [48]), whereas in the case of Al it was fixed at 15 nm due to its higher absorption [49]. The variation in the thickness of the Si_3N_4 layer (d_{SiN} = 250 nm and 180 nm for $x = 0$ and 1, respectively) was chosen in order

to shift the spectral positions of the resonance peaks, thus realizing sensitive regions in the widest spectral domain possible.

The simulated $\Psi = \tan^{-1}(|r_p|/|r_s|)$ spectra for $x = 0,1$ in the KR-configuration are presented in the bottom part of Fig. 1. Here Ψ denotes one of the ellipsometric angles, while r_p and r_s are the amplitude reflection coefficients for p- and s-polarizations, respectively. It is notable that narrow resonance peaks with both polarizations emerge for both $x = 0$ (pure Al) and 1 (pure Ag) and their spectral positions vary from UV (in case of Al) to the NIR range. It is important to emphasize that SPPs cannot be enhanced below ≈300 nm in case of Ag due to its interband transitions. However, for Al the interband transition is a spectrally localized band around 800 nm and surface plasmon resonances can be realized at wavelengths higher or shorter than this value [49,50]. The dashed black lines in Fig. 1 show the TMM-simulated spectra for the scenario when the combinatorial Ag_xAl_{1-x} is not present ($d_{Ag_xAl_{1-x}} = 0$), emphasizing the profound effect of the metallic layer.

Further simulation calculations and results are also included in the Supporting information of present study.

2.3. Spectroscopic ellipsometry

Spectroscopic ellipsometry (SE) is an attractive tool for thin film characterization [51]. This method is based on the measurement of both the amplitude- and phase changes of the light, which is detected after its reflection on the surface of a sample. From a measurement the ellipsometric angles, Ψ and Δ are usually presented being defined by $\rho = \tan\Psi \exp(i\Delta) = r_p/r_s$, where ρ is the complex reflectance ratio [52]. The angles Ψ and Δ are related to the amplitude ratio and the phase difference between p- and s-polarized light, respectively.

The 25 mm × 10 mm sample was placed in a home-built KR-cell which consists of a FS hemicylinder. Using SE and KR-configuration together is a popular method with applications mainly in studies of real-time biological processes [53,54]. Previously it was demonstrated that by using the same setup with a dielectric Bloch-multilayer structure, the ultraviolet wavelength range is also accessible in the reflected spectra [55]. The sample was scanned by a Woollam M-2000DI rotating compensator spectroscopic ellipsometer with a focused spot that was moved along the center line, parallel to the long edge of the sample. The measurements were carried out using a lateral resolution of 1 mm. The plane of incidence was parallel to the short edge, and the AOI was varied between 45° and 75°. The corresponding size of the focused spot was 0.3 mm wide and 0.6–0.9 mm long. The measurement time was a few seconds for one point and one AOI in the whole wavelength range of 250 nm–1690 nm. As a result of the applied technique we obtained, within reasonable time, high-resolution and high-accuracy maps of optical properties as a function of composition and wavelength. The spectral resolution bandwidth is around 5 nm and 10 nm in the UV/Vis and in the NIR wavelength ranges, respectively. The spectral density of the experimental data points is about 1.6 nm and 3.4 nm in the UV/Vis and in the NIR wavelength ranges, respectively.

The optical properties and thicknesses of the combinatorial metal layer were calculated from the measured spectra detected by SE in the KR-configuration. This method is of superior sensitivity [56] when compared to a simple measurement as illustrated with the calculated differential spectra in Fig. 2. Here the difference spectra of Ψ are presented for a 1-nm-change in the Al (15 nm → 16 nm) and Ag (35 nm → 36 nm) layers. It is notable that the spectral changes are significantly larger for the KR-configuration, thus measuring the optical properties in the KR-setup is definitely advantageous.

An optical model of multiple layers was constructed for an appropriate sample analysis. First, the optical properties of the Si_3N_4 layer were calculated by using the $n(\lambda) = A + B/\lambda^2 + C/\lambda^4$ Cauchy-dispersion approach. Here λ corresponds to the incident wave in vacuum in unit of μm, the parameter A is dimensionless, while B and C are in the units of μm^2 and μm^4, respectively. For this investigation a 100-nm-thin Si_3N_4 layer was deposited on a Si substrate and was measured by SE. The calculated parameter values ($A = 1.903$, $B = 0.007$ μm^2 and $C = 0.0005$ μm^4) were then fixed during further data analysis. The optical properties of the Ag_xAl_{1-x} layer were described by the Drude–Lorentz (DL) oscillator model [57,58]. The formalism for the Drude term in the DL model was given by Ref. [59]

$$\varepsilon(E) = \varepsilon_{Drude}(E) + \varepsilon_{Lorentz}(E) = \frac{-\hbar^2}{\varepsilon_0 \rho(\tau E^2 + i\hbar E)} + \sum_{j=1}^{N_{osc}} \frac{A_{Lj} B_{Lj} E_{Lj}}{E_{Lj}^2 - E^2 - iEB_{Lj}},$$

where ρ [Ω cm], τ [s], $\hbar$ [eV s], ε_0 [F cm^{-1}] and N_{osc} are the resistivity, the mean scattering time, the reduced Planck's constant, the permittivity of the free space and the number of oscillators, respectively. In the second term A_L, B_L and E_L are the dimensionless amplitude, the broadening and the central energy (both in eV) of the Lorentzian oscillator. Here j denotes the jth oscillator. During the fit process it was found that for the Ag-rich layers an approach using Gauss-oscillators gave better results [60]. The shape of $\varepsilon_{Gauss}(E)$ was then defined as

$$\varepsilon_{Gauss}(E) = A_{Gj} \cdot \left[\Gamma_{Gj}\left(\frac{E - E_{Gj}}{\sigma_{Gj}}\right) + \Gamma_{Gj}\left(\frac{E + E_{Gj}}{\sigma_{Gj}}\right) + i\left(\exp\left\{-\left(\frac{E - E_{Gj}}{\sigma_{Gj}}\right)^2\right\} - \exp\left\{-\left(\frac{E + E_{Gj}}{\sigma_{Gj}}\right)^2\right\}\right)\right],$$

where E is the photon energy of incident light in eV, $\sigma_G = Br_G/2\sqrt{(\ln 2)}$. Here, A_G is the amplitude, E_G is the center energy in eV and Br_G is the broadening in eV. Γ_G is a convergence series that produces a line shape for ε_1 in a Kramers–Kronig consistent manner [61].

During the data evaluation the sensitive oscillator parameters and thicknesses of the top two layers were fitted. The fitted values were calculated by minimizing the root mean square error (RMSE) defined by Ref. [62]

$$\mathrm{RMSE} = \sqrt{\frac{1}{2M - P - 1}\sum_{j=1}^{M}\left[\left(\frac{\Delta_j^{meas} - \Delta_j^{calc}}{\sigma_{\Delta_j}^{meas}}\right)^2 + \left(\frac{\Psi_j^{meas} - \Psi_j^{calc}}{\sigma_{\Psi_j}^{meas}}\right)^2\right]}, \quad (1)$$

where M is the number of wavelengths, P denotes the number of unknown parameters, while the subscripts '*meas*' and '*calc*' indicate the measured and calculated values. Here σ is the standard deviation of the measured values. A global fit on random grid with Levenberg–Marquardt algorithm [63] was used for obtaining the global minimum during the fitting process.

The RMSE values were carefully investigated and compared for both the Lorentzian- and Gaussian-approaches and it was found that starting from the Al side ($x = 0$) to $x \approx 0.4$ the Drude–Lorentz model produces better results.

2.4. Transmission electron microscopy

The microstructure of the sensor was investigated by transmission electron microscopy (TEM), high resolution TEM (HRTEM), scanning TEM (STEM), high angle annular dark field (HAADF) and energy dispersive X-ray spectrometry (EDS) modes by means of a FEI Titan Themis 200 kV spherical aberration (Cs) corrected TEM with 0.09 nm HRTEM and 0.16 nm STEM resolution. The composition of the samples was measured by STEM–EDS and elemental maps were obtained by spectrum imaging with 4 Thermo-Fischer "Super X G1" EDS detectors built in the microscope column.

3. Results and discussion

3.1. Properties of the Ag_xAl_{1-x} layer characterized by SE and TEM

TEM measurements were carried out on FIB cross section lamellae prepared at four selected positions along the combinatorial sample,

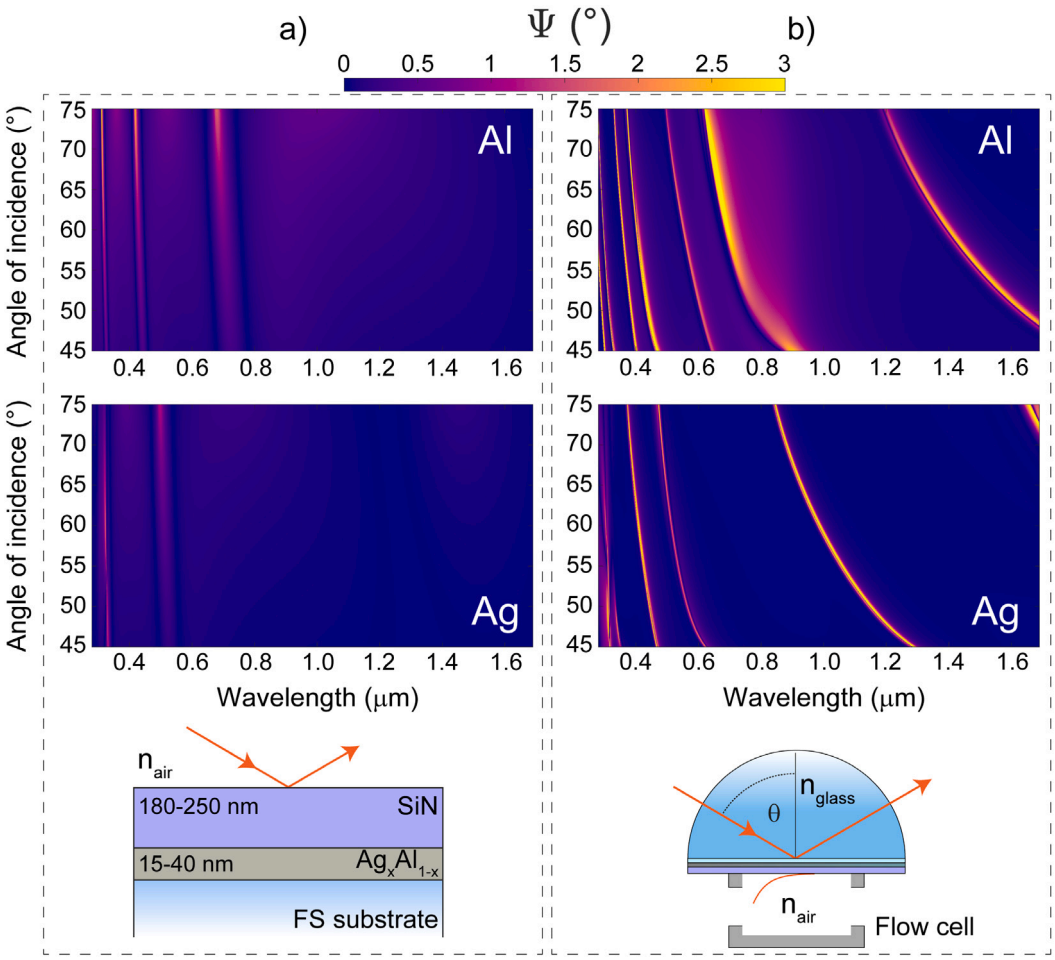

Fig. 2. The simulated effect of a 1-nm thickness change in the Ag_xAl_{1-x} layer at $x = 0$ and 1 using reflection configurations measuring from (a) the ambient and (b) from the substrate (KR-configuration).

representing different x compositions and thicknesses of the Ag_xAl_{1-x} and Si_3N_4 layers. Fig. 3 represents the TEM results achieved at a position of 9.5 mm along the sample ($x \approx 0.65$).

TEM and SEM HAADF micrographs of the cross-section of the sample taken at the above position shown in Fig. 3a and b revealed a thickness of 32 nm and 225 nm for the Ag_xAl_{1-x} and Si_3N_4 layers, respectively. EDS measurement of the Ag_xAl_{1-x} layer at the same position showed a composition of Ag/Al = 65/35 in terms of atomic percent. The elemental map and an EDS line-scan across the layer system including silica/Ag_xAl_{1-x}/Si_3N_4/C+Pt(C) are shown in Fig. 3c and d. In the line-scan, HAADF appearing in black shows the Z-contrast change across the layers.

The thicknesses of the combinatorial metal layer and the Si_3N_4 films were characterized by SE measurements in the KR-configuration and by TEM measurements. The result of this analysis is shown in Fig. 4a. It is very conclusive that the measured thickness values from the SE and TEM investigations are in excellent agreement, while they are also close to the planned values along the samples. Besides the thickness values the compositions of Al and Ag were also obtained by TEM. The results presented in Fig. 4b indicate that the planned linearity of composition dependence was successfully achieved.

3.2. Composition dependence of the optical properties of the Ag_xAl_{1-x} layer

SE investigation of the Ag_xAl_{1-x}/Si_3N_4 structure was carried out parallel to the long edge of the sample with a lateral resolution of 1 mm in the KR-cell filled with air. The measured Ψ-spectra at $\theta = 47°$ is presented in Fig. 5a across the λ range of 250–1690 nm. From this investigation, significant spectral changes are obtained regarding the positions and the FWHM values of the resonances indicating the huge effect of the variable metal composition. Detailed Ψ spectra were also captured for $\theta = 45$–$55°$ and presented at $x \approx 0$ and 1 in Fig. 5b. The AOI step in these figures is 0.2°.

The significance of shifting the spectral position of the resonance peaks by simply changing the position of the light spot along the sample can be advantageous for optical sensing arrangements where the AOI cannot be changed. In the case of pure Ag it is also true that regardless the AOI, resonance peak positions have a lower limit regarding the accessible smallest wavelength value which can be further reduced only by modulating its optical properties. Also, the change of AOI usually deteriorates the broadening to a larger extent than the change of composition. Finally, there are wavelength ranges that are not accessible by changing the AOI.

The composition dependent dielectric functions were calculated from the fitted (Ψ, Δ) spectra that were measured in the KR-cell (Typical spectra are shown in Fig. 5c). In this analysis the oscillator parameter values and the thicknesses of the Ag_xAl_{1-x}/Si_3N_4 layers were fitted. The obtained complex dielectric functions are presented in Fig. 6. In Fig. 6a and b optical functions from $x \approx 1$ to $x \approx 0.4$ are depicted. It is to be noted that ε_2 increases when x decreases. This can be explained by the increasing amount of the Al impurities (greater electron scattering due to compositional disorder in the system) [29,64]. The blue-shift of the interband transitions by decreasing x is also a well-known effect [64] as well as the appearance of a new ε_2-peak near 500 nm. This latter phenomenon can be attributed to new interband transitions [65].

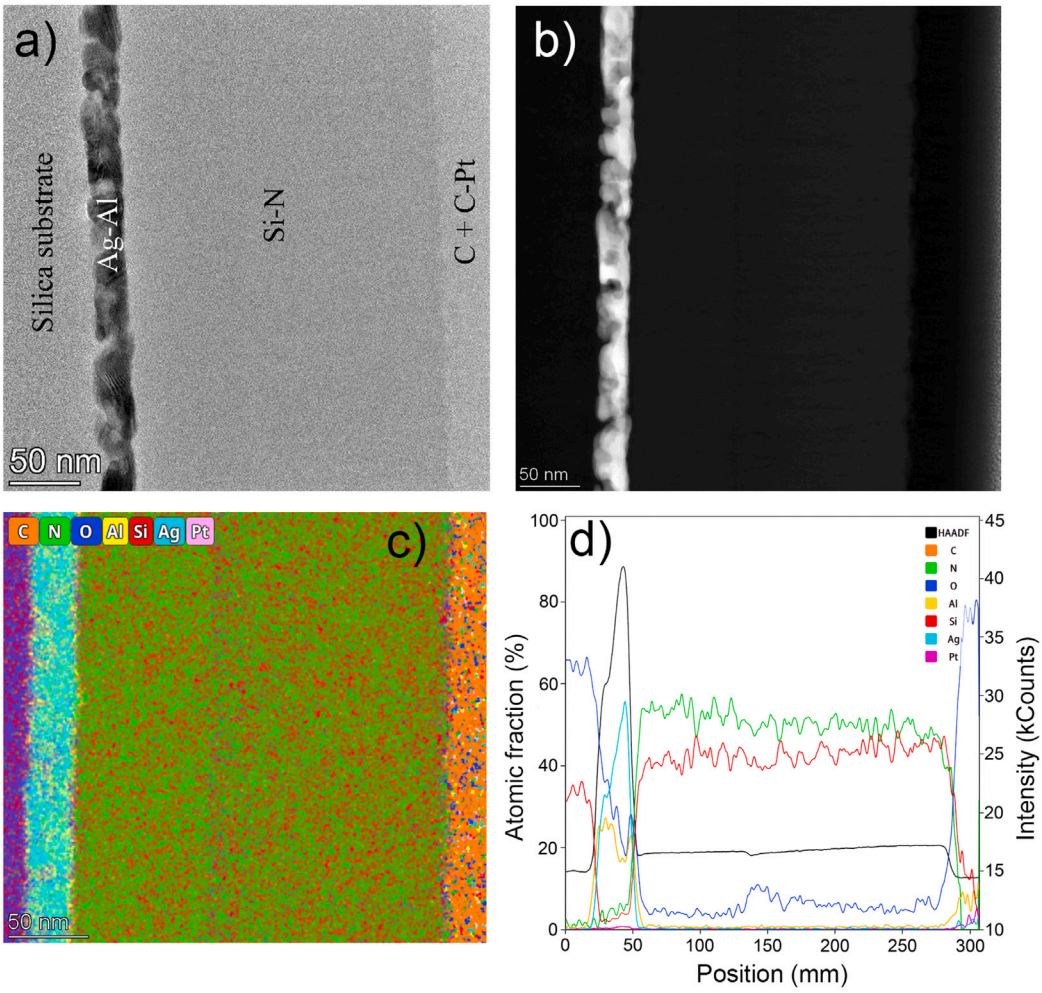

Fig. 3. Cross section TEM of the sample at the position of Ag/Al = 65/35 at.%. (a,b) TEM and SEM HAADF image, respectively, (c) Colored EDS elemental map of the cross section of the sample, (d) A line-scan of the compositional changes (at%) across the layer system: Silica/Ag_xAl_{1-x}/Si_3N_4/C+PtC.

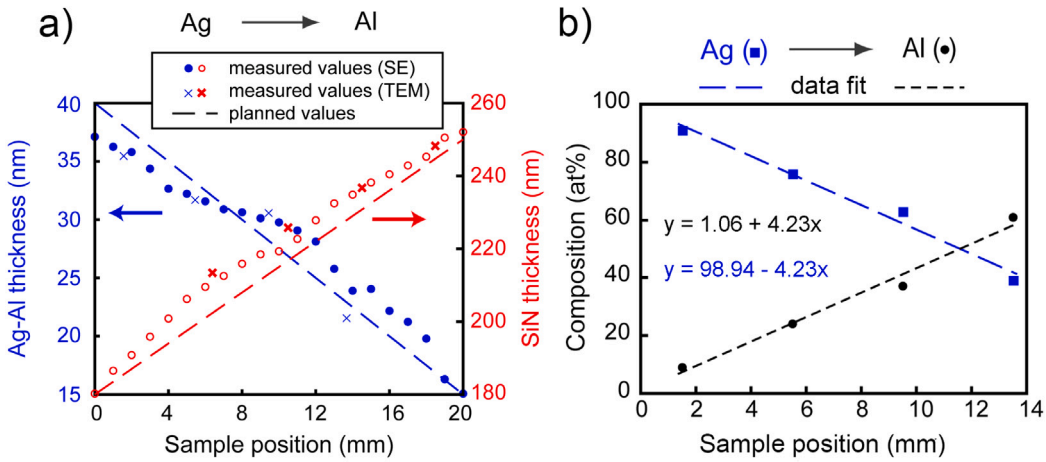

Fig. 4. (a) Measured Ag_xAl_{1-x} and Si_3N_4 thicknesses along the sample from TEM and SE experiments. The dashed lines denote the desired trends. (b) Measured position-dependence of the Ag_xAl_{1-x} composition by TEM-FIB investigations.

Starting from the Al-rich side ($x \approx 0$), a significant change in ε_2 can be observed once again. Here, the ε_2-peak shifts toward the smaller wavelengths as well and it can be noticed that in the NIR wavelength range the value of ε_2 decreases by the increasing value of x. In fact, the interband transition peak shifts from 740 nm ($x \approx 0$) to 485 nm ($x \approx 0.35$).

For the elucidation of these results it is vital to emphasize that not only the composition x but also the thickness of the combinatorial layer changes, which bears a huge effect on the optical properties [66–68]. Besides the crystallites/grain shape and size of metal films, it is well-known that thickness can also significantly influence the optical properties when it is smaller than approximately 50 nm [69]. This

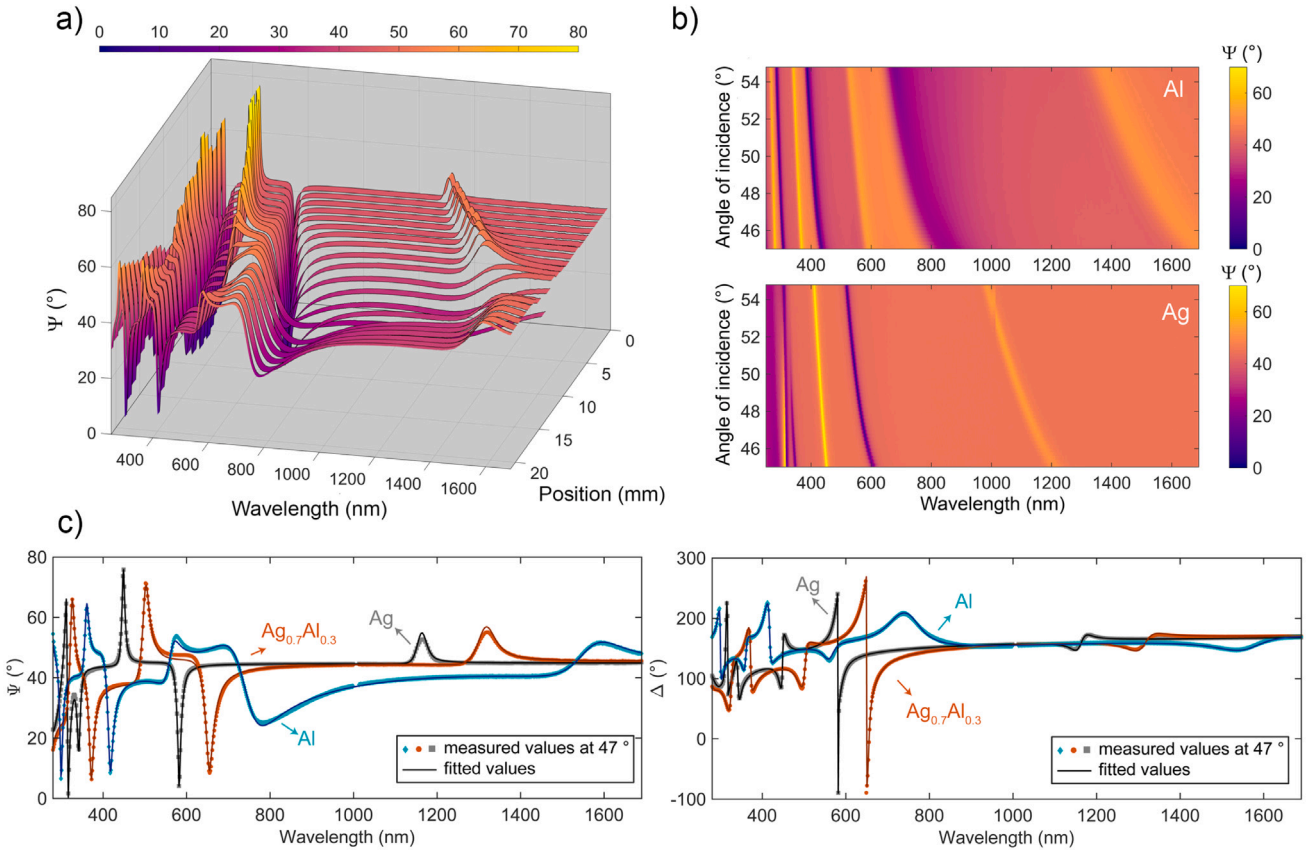

Fig. 5. (a) Measured Ψ-spectra along the combinatorial sample in the wavelength range of 250–1690 nm and at $\theta = 47°$. (b) Measured Ψ-spectra at $x \approx 0$ and 1 (Al and Ag in the top and bottom figures, respectively), at $\theta = 45° - 55°$. (c) Typical measured Ψ and Δ spectra at $\theta = 47°$ with fitted curves.

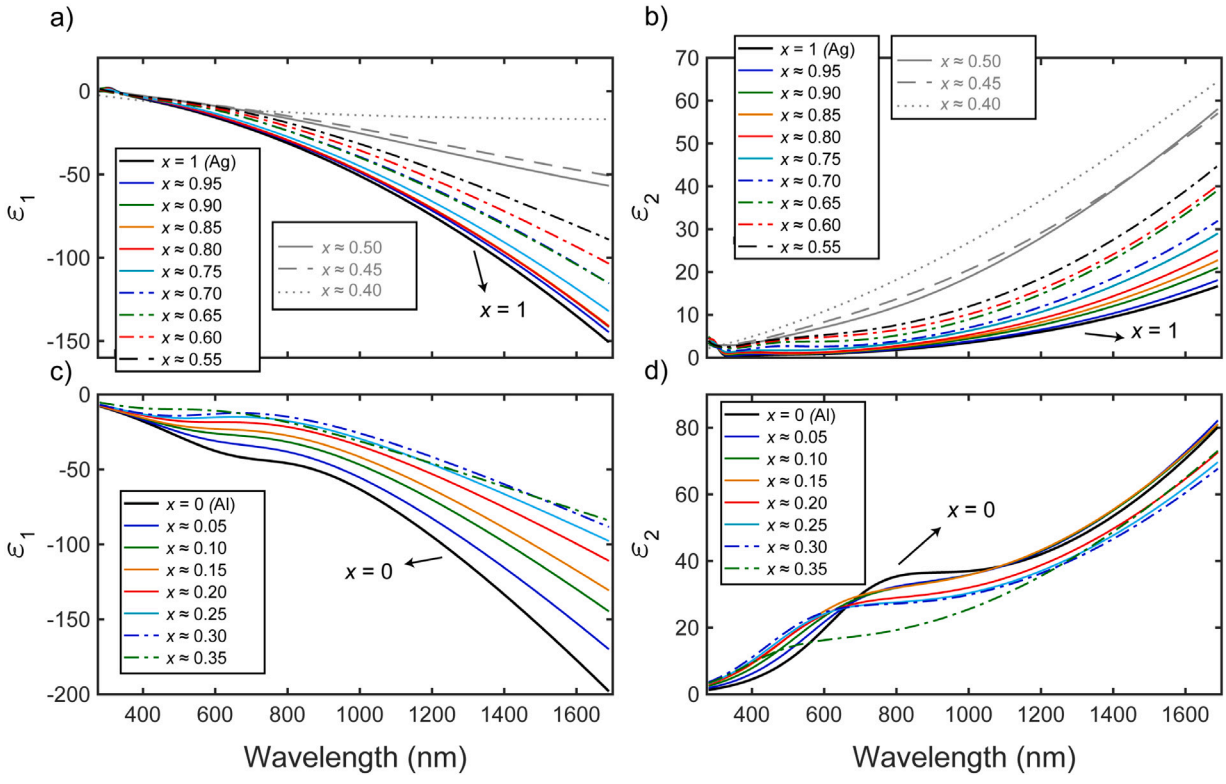

Fig. 6. (a) and (c) ε_1, (b) and (d) ε_2 values from SE measurements in the KR cell.

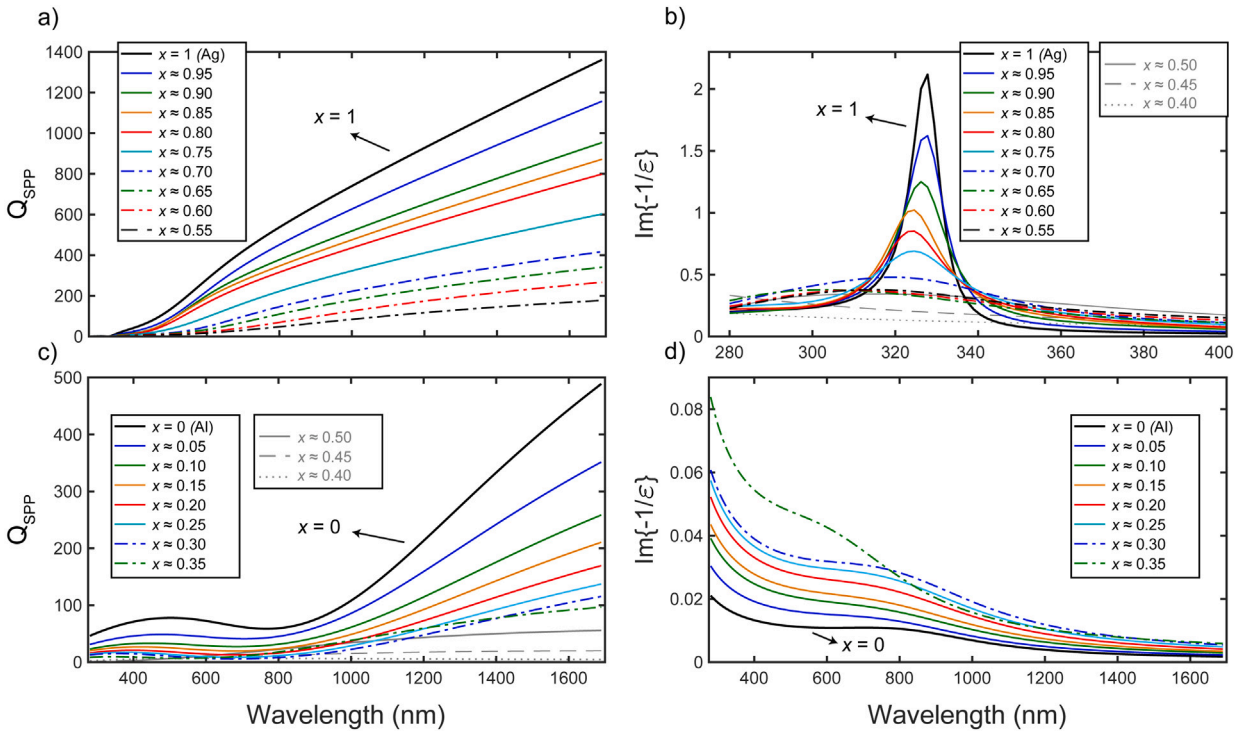

Fig. 7. (a) and (c) Calculated Q_{SPP}, (b) and (d) calculated Im$\{-1/\varepsilon\}$ values from SE measurements. Note that the layer thickness is not constant for the different compositions.

effect can be attributed to the fact that the typical value of the average path of free electrons in Ag ($l = 4.375 \cdot 10^{-8}$ m [70]) is then comparable to the typical size of the crystallites. Consequently the grains size affects the average free path of the electrons and for this reason the values of and the so called free electron effect will be observable [71].

Meanwhile, it has also been shown previously that the circumstances of Al layer deposition via various techniques also have a profound influence on the dielectric function of the film since it can influence the typical grain size within a wide range (ca. 10–50 nm) [72–74].

According to the measured Ψ-spectra and the results from the optical analysis, layers with compositions $x \approx 0.40$, 0.45 and 0.50 have the most different features among the measured points. In this x-range dielectric functions were described either by a single Drude-oscillator ($x \approx 0.4$) or with a Drude-Gauss approach ($x \approx 0.45, 0.50$). This phenomenon in the mentioned x composition range may be attributed to the phase changes described in Ref. [75].

For planar SPR applications a quality factor can be defined as $Q_{SPP} = \varepsilon_1^2/\varepsilon_2$ [76] (SPP stands for surface plasmon polariton). Calculation of Q_{SPP} can be useful for identifying the most sensitive x composition for a given wavelength range. From Ref. [17] it is evident that among various candidates Ag has the highest Q_{SPP} value ranging up to $\lambda = 10$ μm. However, for UV applications Al is the best choice, Q_{SPP}^{Al} being between 10 and 100 in this wavelength range. This value is highly dependent on the layer thickness of the metal layer due to its effect on the optical losses. However, it is apparent from Fig. 7c that the value $Q_{SPP}^{Al} \approx 100$ can be achieved. For Ag the Q_{SPP} value is approximately three times higher in the IR range with respect to Al (Fig. 7a). It can be noticed that the highest Q_{SPP} values were achieved for $x \approx 1$. However, for $x \approx 0.95$ the decrease in Q_{SPP} can be still tolerated.

In Fig. 7b and d the x composition dependence of the Im$\{-1/\varepsilon\} = \varepsilon_2/(\varepsilon_1^2+\varepsilon_2^2)$ energy loss function is depicted that can be used for indicating the existence of electronic collective oscillators. The maximum of the Im$\{-1/\varepsilon\}$ value indicates plasma resonances in the materials [65] near to the interband transitions at 325 nm in Ag ($x = 1$). By decreasing x the value of the maximum decreases and its spectral position is blue-shifted. These trends in the results are similar to the ones that have been found for Ag-Al [64,77] and for Ag–Cu alloys earlier [14]. Starting from $x = 0$ (Al) Im$\{-1/\varepsilon\}$ is increasing with x, which is an opposite effect than in previous results [32]. However, in the same study it was found that by increasing the layer thickness, Im$\{-1/\varepsilon\}$ also increases, which in this case seems to be the dominant effect.

3.3. Ag_xAl_{1-x} layer for optical sensor applications

The fabricated sensor structure has optimized thicknesses only at compositions $x = 0$ (pure Al) and $x = 1$ (pure Ag), because the optical properties of these pure phases were considered to be more reliable than the references for mixed phases. After the determination of the optical properties for all the x values, it would be possible to optimize the lateral thickness profile, but our one-sample combinatorial device is currently only optimized for linearly graded compositions and thicknesses. The utilization of both arbitrary composition and thickness profiles can be a next step in the development process, published in a following paper.

To demonstrate the sensitivities of the ellipsometic angles at both $x = 0$ and $x = 1$, results from TMM-calculations are presented in Fig. 8. The spectral differences in both Ψ and Δ were calculated in the wavelength range of 250–1700 nm and the AOI range of 40–75°. The shift in the spectra stemmed from a $\Delta n_{air} = 10^{-3}$ refractive index change in the ambient air. Sensitive regions emerge for both layer structures making them ideal candidates for gas-sensing applications. (The differences in the spectra presented in Figs. 1 and 8 are due to the different n_{FS} values being used in the simulations. For Fig. 1 $n_{FS} = 1.5$ without any dispersion, while for Fig. 8 n_{FS} was described by using the Sellmeier term imported from Ref. [55]. The origin of the resonance peaks are the same as described earlier, however, their spectral positions are slightly shifted.)

The same calculations were also computed in an aqueous ambient for $\theta = 65$–75° (Fig. 9). Here, the refractive index of water (n_{water}) was chosen to be 1.312 and its change was $\Delta n_{water} = 10^{-4}$. A theoretical limit of detection (LOD) value was estimated (by using a typical noise

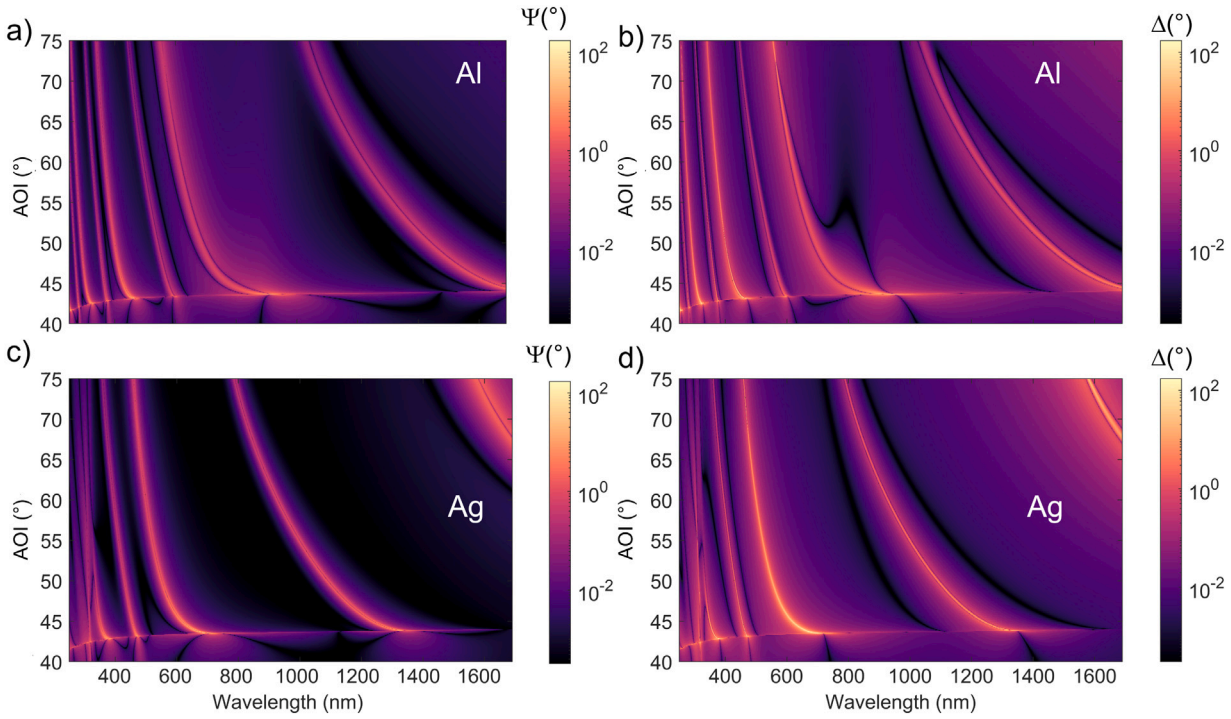

Fig. 8. TMM-calculated differences in (Ψ, Δ) spectra for a $\Delta n_{air} = 10^{-3}$ change. Sub-figures (a) and (b) stand for Al, while sub-figures (c) and (d) for Ag.

value σ_{meas} from a real measurement) from these results as the smallest detectable bulk refractive index change using the expression LOD = $3{\cdot}\sigma_{meas}/S$. Here, S denotes the sensitivity defined as $S = \Delta\Delta/\Delta n_{water}$. (Since the sensitivity of Δ is usually higher than that of Ψ, thus in this analysis all values were calculated using the phase information.) The calculated LOD values for the Al and Ag sample positions are $\mathrm{LOD}_{Al} = 5.0 \cdot 10^{-6}$ and $\mathrm{LOD}_{Ag} = 2.5 \cdot 10^{-6}$ in refractive index units (RIU), respectively. From these results we can conclude that the realized structure is an excellent candidate for biosensing applications, with resonance peaks at multiple spectral positions, which opens further possibilities in the domain of investigations of real-time protein adsorption.

Measurements at $x = 0$ and 1 were also carried out for demonstrating the sensitivity of the structure at $\theta = 73°$ (Fig. 10c and d). Solutions of high-purity deinonized (DI) water and isopropanol (VWR Chemicals) with various concentrations (2.5%, 5%, 7.5% and 10%) were introduced to the flow cell, with different refractive indices of $n_{isoprop.}^{2.5\%\ldots10\%} = 1.3324$, 1.3339, 1.3356, 1.3376 and 1.3390, respectively (obtained from refractometric measurements at $\lambda = 632$ nm and at room temperature). In the following, subscripts 1, 2, 3, and 4 are used to label the refractive indices of various concentrations of 2.5%, 5%, 7.5% and 10%, respectively. The difference spectra measured in the KR-cell are presented in Fig. 10c and d for both ellipsometric angles. It is evident that Δ is more sensitive than Ψ, since the change is almost one-order of magnitude larger. For $n_{21} = 1.6 \times 10^{-3}$ RIU the biggest $\Delta\Delta_{21}^{Ag}$ difference for $x = 1$ is 70.05° positioned at $\lambda = 535.4$ nm, and $\Delta\Delta_{21}^{Al} = 36.38°$ at $\lambda = 685.7$ nm. From these results the LOD_{Ag}^{meas} can be estimated to be $4.1 \cdot 10^{-6}$ RIU and $\mathrm{LOD}_{Al}^{meas} = 7.9 \cdot 10^{-6}$ RIU.

The TMM-simulated results (Fig. 10a and b] show similar sensitivities. However, regarding the peak for $x = 1$ near $\lambda \approx 1000$ nm and for the UV-peaks for $x = 0$, higher sensing performance are predicted by the numerical calculations. This decrease in the performance can be attributed to various effects such as the emerging depolarization stemming from e.g., the angular spread of the incident light [55] or the inhomogeneity of layer thicknesses/compositions (e.g., latter being ≈1.5% for Ag_xAl_{1-x} thin film) of the combinatorial layers under the light spot. Besides that the non-optimal performance of the deuterium lamp at these wavelengths also can have a significant effect on the sensitivities. Typical depolarization spectra from measurement are depicted in Fig. 6S.

Conclusions

In this study a combinatorial thin layer structure was introduced which is capable of the optical detection of minute changes in the refractive index of gas or liquid ambient. The combinatorial sample consists of an Ag_xAl_{1-x}/Si_3N_4 layer structure which was deposited on a FS glass slide by dual DC magnetron sputtering. It was shown that not only the composition can be covered in the whole range of $(0 \le x \le 1)$, but also the thickness of the Ag_xAl_{1-x} and Si_3N_4 layers can be tuned along a single sample. The optical properties of the combinatorial layer were characterized by KR SE from which the composition dependent trends in both ε_1 and ε_2 were obtained. These changes agree well with previously reported literatures; although this is the first study where ε is reported in the whole x range.

The sensing properties of the structure were also investigated numerically (at composition values of $x = 0$ and 1) for gas sensing applications and for biosensing applications in a liquid ambient. Based on the results it was verified that the realized structure is capable of highly sensitive detection in the UV–Vis–NIR wavelength ranges at a single AOI. Ellipsometric phase-sensitive measurements were also carried out from which detection limit values of $4.1 \cdot 10^{-6}$ RIU and $7.9 \cdot 10^{-6}$ RIU were measured at the Ag- and Al-sides of the chip. Our multi-spot, multi-angle tool with the compositionally graded surface realizes a "scanning resonant wavelength" capability, in which the spectral position of the highest sensitivity can be adjusted during the in-situ measurement.

CRediT authorship contribution statement

Benjamin Kalas: Conceptualization, Data curation, Formal analysis, Investigation, Methodology, Validation, Writing – original draft, Writing – review & editing. **György Sáfrán:** Methodology, Investigation, Conceptualization. **Miklós Serényi:** Methodology, Investigation, Conceptualization. **Miklós Fried:** Funding acquisition, Project administration, Resources. **Péter Petrik:** Conceptualization, Methodology, Funding acquisition, Project administration, Resources, Investigation, Validation, Writing – original draft, Writing – review & editing.

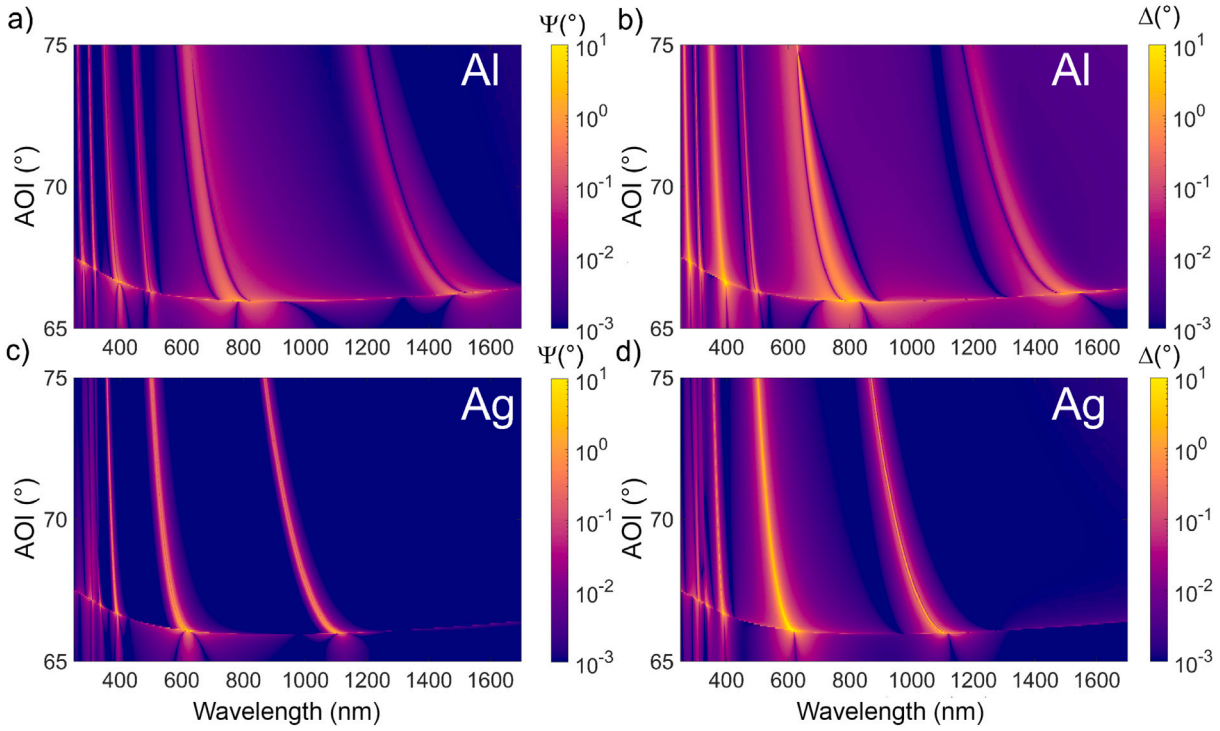

Fig. 9. TMM-calculated differences in (Ψ, Δ) spectra for a $\Delta n_{water} = 10^{-4}$ change. Sub-figures (a) and (b) stand for Al, while sub-figures (c) and (d) for Ag.

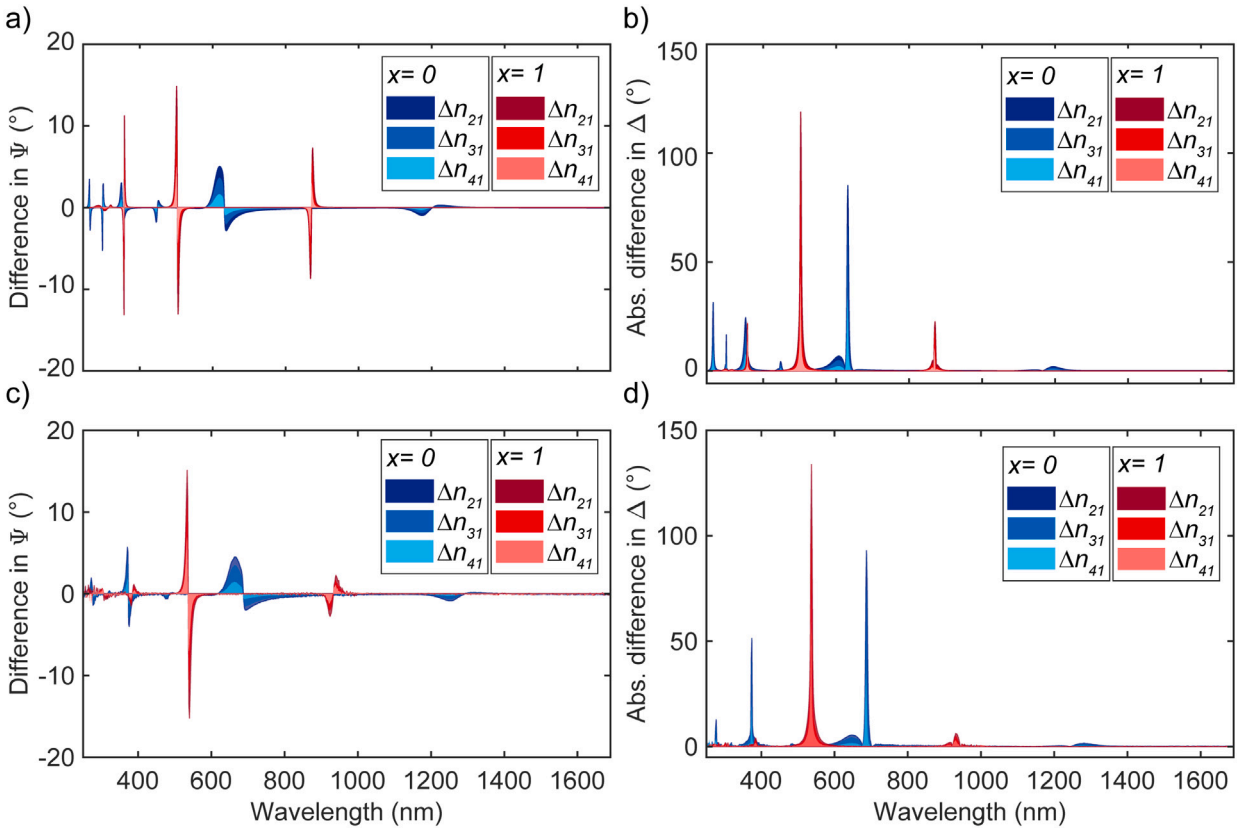

Fig. 10. Difference of simulated [(a) and (b)] and measured [(c) and (d)] Ψ and Δ spectra at compositions $x = 0$ and 1 for various DI water–isopropanol solution ambient. Δn_{j1} denotes the refractive index difference at $\lambda = 632$ nm $(j = 2, 3, 4)$.

Declaration of competing interest

The authors declare that they have no known competing financial interests or personal relationships that could have appeared to influence the work reported in this paper.

Data availability

Data will be made available on request.

Acknowledgments

Support from the National Development Agency Grants of OTKA Nr. K131515 and K129009 are greatly acknowledged. The work in frame of the 20FUN02 "POLight" project has received funding from the EMPIR programme co-financed by the Participating States and from the European Union's Horizon 2020 research and innovation programme. Project no. TKP2021-EGA04 has been implemented with the support provided by the Ministry of Innovation and Technology of Hungary from the National Research, Development and Innovation Fund, financed under the TKP2021 funding scheme.

Appendix A. Supplementary data

Supplementary material related to this article can be found online at https://doi.org/10.1016/j.apsusc.2022.154770.

References

[1] E. Wijaya, C. Lenaerts, S. Maricot, J. Hastanin, S. Habraken, J. Vilcot, R. Boukherroub, S. Szunerits, Surface plasmon resonance-based biosensors: From the development of different SPR structures to novel surface functionalization strategies, Curr. Opin. Solid State Mater. Sci. 15 (2011) 208–224, http://dx.doi.org/10.1016/j.cossms.2011.05.001.

[2] M.R.S. Dias, C. Gong, Z.A. Benson, M.S. Leite, Lithography-free, omnidirectional, CMOS-compatible AlCu alloys for thin-film superabsorbers, Adv. Opt. Mater. 6 (2) (2018) 1700830, http://dx.doi.org/10.1002/adom.201700830, URL: https://onlinelibrary.wiley.com/doi/abs/10.1002/adom.201700830. arXiv:https://onlinelibrary.wiley.com/doi/pdf/10.1002/adom.201700830.

[3] C. Gong, M.S. Leite, Noble metal alloys for plasmonics, ACS Photon. 3 (4) (2016) 507–513, http://dx.doi.org/10.1021/acsphotonics.5b00586, arXiv:https://doi.org/10.1021/acsphotonics.5b00586.

[4] J.P. McClure, J. Boltersdorf, D.R. Baker, T.G. Farinha, N. Dzuricky, C.E.P. Villegas, A.R. Rocha, M.S. Leite, Structure–property-performance relationship of ultrathin pd–au alloy catalyst layers for low-temperature ethanol oxidation in alkaline media, ACS Appl. Mater. Interfaces 11 (28) (2019) 24919–24932, http://dx.doi.org/10.1021/acsami.9b01389, arXiv:https://doi.org/10.1021/acsami.9b01389, PMID: 31044596.

[5] C. Gong, A. Kaplan, Z.A. Benson, D.R. Baker, J.P. McClure, A.R. Rocha, M.S. Leite, Band structure engineering by alloying for photonics, Adv. Opt. Mater. 6 (17) (2018) 1800218, http://dx.doi.org/10.1002/adom.201800218, URL: https://onlinelibrary.wiley.com/doi/abs/10.1002/adom.201800218. arXiv:https://onlinelibrary.wiley.com/doi/pdf/10.1002/adom.201800218.

[6] M. Rebello Sousa Dias, M.S. Leite, Alloying: A platform for metallic materials with on-demand optical response, Acc. Chem. Res. 52 (10) (2019) 2881–2891, http://dx.doi.org/10.1021/acs.accounts.9b00153, arXiv:https://doi.org/10.1021/acs.accounts.9b00153, PMID: 31305980.

[7] P. West, S. Ishii, G. Naik, N. Emani, V. Shalaev, A. Boltasseva, Searching for better plasmonic materials, Laser Photonics Rev. 4 (6) (2010) 795–808, http://dx.doi.org/10.1002/lpor.200900055, URL: https://onlinelibrary.wiley.com/doi/abs/10.1002/lpor.200900055. arXiv:https://onlinelibrary.wiley.com/doi/pdf/10.1002/lpor.200900055.

[8] A. Bouhelier, T. Huser, H. Tamaru, H.-J. Güntherodt, D.W. Pohl, F.I. Baida, D. Van Labeke, Plasmon optics of structured silver films, Phys. Rev. B 63 (2001) 155404, http://dx.doi.org/10.1103/PhysRevB.63.155404, URL: https://link.aps.org/doi/10.1103/PhysRevB.63.155404.

[9] R.E. Peale, O. Lopatiuk, J. Cleary, S. Santos, J. Henderson, D. Clark, L. Chernyak, T.A. Winningham, E.D. Barco, H. Heinrich, W.R. Buchwald, Propagation of high-frequency surface plasmons on gold, J. Opt. Soc. Amer. B 25 (10) (2008) 1708–1713, http://dx.doi.org/10.1364/JOSAB.25.001708, URL: http://josab.osa.org/abstract.cfm?URI=josab-25-10-1708.

[10] L. Zhou, Y. Tan, J. Wang, W. Xu, Y. Yuan, W. Cai, S. Zhu, J. Zhu, 3D self-assembly of aluminium nanoparticles for plasmon-enhanced solar desalination, Nature Photon. 10 (2016) http://dx.doi.org/10.1038/nphoton.2016.75.

[11] C. Haffner, D. Chelladurai, Y. Fedoryshyn, A. Josten, B. Baeuerle, W. Heni, T. Watanabe, T. Cui, B. Cheng, S. Saha, D. Elder, L. Dalton, A. Boltasseva, V. Shalaev, N. Kinsey, J. Leuthold, Low loss plasmon-assisted electro-optic modulator, Nature 556 (2018) http://dx.doi.org/10.1038/s41586-018-0031-4.

[12] X. Deng, L. Li, M. Enomoto, Y. Kawano, Continuously frequency-tuneable plasmonic structures for terahertz bio-sensing and spectroscopy, Sci. Rep. 9 (1) (2019) 3498, http://dx.doi.org/10.1038/s41598-019-39015-6.

[13] D.A. Bobb, G. Zhu, M. Mayy, A.V. Gavrilenko, P. Mead, V.I. Gavrilenko, M.A. Noginov, Engineering of low-loss metal for nanoplasmonic and metamaterials applications, Appl. Phys. Lett. 95 (15) (2009) 151102, http://dx.doi.org/10.1063/1.3237179, arXiv:https://doi.org/10.1063/1.3237179.

[14] G. Yang, X. Fu, J. Zhou, Dielectric properties of the silver-copper alloy films deposited by magnetron sputtering, J. Opt. Soc. Amer. B 30 (2) (2013) 282–287, http://dx.doi.org/10.1364/JOSAB.30.000282, URL: http://josab.osa.org/abstract.cfm?URI=josab-30-2-282.

[15] O. Peña-Rodríguez, M. Caro, A. Rivera, J. Olivares, J.M. Perlado, A. Caro, Optical properties of au-ag alloys: An ellipsometric study, Opt. Mater. Express 4 (2) (2014) 403–410, http://dx.doi.org/10.1364/OME.4.000403, URL: http://www.osapublishing.org/ome/abstract.cfm?URI=ome-4-2-403.

[16] R. Collette, Y. Wu, A. Olafsson, J.P. Camden, P.D. Rack, Combinatorial thin film sputtering Au_xAl_{1-x} alloys: Correlating composition and structure with optical properties, ACS Combin. Sci. 20 (11) (2018) 633–642, http://dx.doi.org/10.1021/acscombsci.8b00091, arXiv:https://doi.org/10.1021/acscombsci.8b00091, PMID: 30277750.

[17] M.G. Blaber, M.D. Arnold, M.J. Ford, A review of the optical properties of alloys and intermetallics for plasmonics, J. Phys.: Condens. Matter 22 (14) (2010) 143201, http://dx.doi.org/10.1088/0953-8984/22/14/143201.

[18] G. Subramania, A.J. Fischer, T.S. Luk, Optical properties of metal-dielectric based epsilon near zero metamaterials, Appl. Phys. Lett. 101 (24) (2012) 241107, http://dx.doi.org/10.1063/1.4770517, arXiv:https://doi.org/10.1063/1.4770517.

[19] R. Lazzari, J. Jupille, Silver layers on oxide surfaces: morphology and optical properties, Surf. Sci. 482–485 (2001) 823–828, http://dx.doi.org/10.1016/S0039-6028(01)00935-9, URL: https://www.sciencedirect.com/science/article/pii/S0039602801009359.

[20] D.-T. Nguyen, S. Vedraine, L. Cattin, P. Torchio, M. Morsli, F. Flory, J.C. Bernède, Effect of the thickness of the MoO_3 layers on optical properties of MoO_3/Ag/MoO_3 multilayer structures, J. Appl. Phys. 112 (6) (2012) 063505, http://dx.doi.org/10.1063/1.4751334, arXiv:https://doi.org/10.1063/1.4751334.

[21] R.S. Sennett, G.D. Scott, The structure of evaporated metal films and their optical properties, J. Opt. Soc. Amer. 40 (4) (1950) 203–211, http://dx.doi.org/10.1364/JOSA.40.000203, URL: http://www.osapublishing.org/abstract.cfm?URI=josa-40-4-203.

[22] V.J. Logeeswaran, N.P. Kobayashi, M.S. Islam, W. Wu, P. Chaturvedi, N.X. Fang, S.Y. Wang, R.S. Williams, Ultrasmooth silver thin films deposited with a germanium nucleation layer, Nano Lett. 9 (1) (2009) 178–182, http://dx.doi.org/10.1021/nl8027476, arXiv:https://doi.org/10.1021/nl8027476, PMID: 19105737.

[23] J. Zhang, D.M. Fryauf, M. Garrett, V. Logeeswaran, A. Sawabe, M.S. Islam, N.P. Kobayashi, Phenomenological model of the growth of ultrasmooth silver thin films deposited with a germanium nucleation layer, Langmuir 31 (28) (2015) 7852–7859, http://dx.doi.org/10.1021/acs.langmuir.5b01244, arXiv:https://doi.org/10.1021/acs.langmuir.5b01244, PMID: 26126182.

[24] M. Fahland, P. Karlsson, C. Charton, Low resisitivity transparent electrodes for displays on polymer substrates, Thin Solid Films 392 (2) (2001) 334–337, http://dx.doi.org/10.1016/S0040-6090(01)01053-7, URL: https://www.sciencedirect.com/science/article/pii/S0040609001010537. 3rd International Conference on Coatings on Glass (ICCG).

[25] C. Zhang, D. Zhao, D. Gu, H. Kim, T. Ling, Y.-K.R. Wu, L.J. Guo, An ultrathin, smooth, and low-loss al-doped ag film and its application as a transparent electrode in organic photovoltaics, Adv. Mater. 26 (32) (2014) 5696–5701, http://dx.doi.org/10.1002/adma.201306091, URL: https://onlinelibrary.wiley.com/doi/abs/10.1002/adma.201306091. arXiv:https://onlinelibrary.wiley.com/doi/pdf/10.1002/adma.201306091.

[26] Q. Hao, D. Du, C. Wang, W. Li, H. Huang, J. Li, T. Qiu, P.K. Chu, Plasmon-induced broadband fluorescence enhancement on al-ag bimetallic substrates, Sci. Rep. 4 (2014) http://dx.doi.org/10.1038/srep06014.

[27] E.D. Palik, Handbook of Optical Constants of Solids, Vol. 1, Acad. Press, San Diego, 1998.

[28] R. Adams, C. Nordin, K. Masterson, Al-ag alloy films for solar reflectors, Thin Solid Films 72 (2) (1980) 335–339, http://dx.doi.org/10.1016/0040-6090(80)90015-2, URL: https://www.sciencedirect.com/science/article/pii/0040609080900152.

[29] S. Auer, W. Wan, X. Huang, A.G. Ramirez, H. Cao, Morphology-induced plasmonic resonances in silver-aluminum alloy thin films, Appl. Phys. Lett. 99 (4) (2011) 041116, http://dx.doi.org/10.1063/1.3619840, arXiv:https://doi.org/10.1063/1.3619840.

[30] C. Zhang, N. Kinsey, L. Chen, C. Ji, M. Xu, M. Ferrera, X. Pan, V.M. Shalaev, A. Boltasseva, L.J. Guo, High-performance doped silver films: Overcoming fundamental material limits for nanophotonic applications, Adv. Mater. 29 (19) (2017) 1605177, http://dx.doi.org/10.1002/adma.201605177, URL:

https://onlinelibrary.wiley.com/doi/abs/10.1002/adma.201605177. arXiv:https://onlinelibrary.wiley.com/doi/pdf/10.1002/adma.201605177.
[31] H. Kim, T. Alford, Improvement of the thermal stability of silver metallization, J. Appl. Phys. 94 (8) (2003) 5393–5395.
[32] J. Yang, J. Zhou, Dielectric properties of aluminum silver alloy thin films in optical frequency range, J. Appl. Phys. 109 (12) (2011) 123105, http://dx.doi.org/10.1063/1.3592971, arXiv:https://doi.org/10.1063/1.3592971.
[33] G. Yang, X.-J. Fu, J.-B. Sun, J. Zhou, Optical properties of aluminum silver alloy films deposited by magnetron sputtering, J. Alloys Compd. 547 (2013) 23–28, http://dx.doi.org/10.1016/j.jallcom.2012.08.007, URL: https://www.sciencedirect.com/science/article/pii/S0925838812013928.
[34] K. Diest, V. Liberman, D. Lennon, P. Welander, M. Rothschild, Aluminum plasmonics: Optimization of plasmonic properties using liquid-prism-coupled ellipsometry, Opt. Express 21 (2013) 28638–28650, http://dx.doi.org/10.1364/OE.21.028638.
[35] I. Tanabe, Y. Y. Tanaka, K. Watari, T. Hanulia, T. Goto, W. Inami, Y. Kawata, Y. Ozaki, Far- and deep-ultraviolet surface plasmon resonance sensors working in aqueous solutions using aluminum thin films, Sci. Rep. 7 (2017) 1.
[36] G. Sáfrán, "One-sample concept" micro-combinatory for high throughput TEM of binary films, Ultramicroscopy 187 (2018) 50–55.
[37] D. Sarid, Long-range surface-plasma waves on very thin metal films, Phys. Rev. Lett. 47 (1981) 1927–1930, http://dx.doi.org/10.1103/PhysRevLett.47.1927.
[38] G. Nenninger, P. Tobiška, J. Homola, S. Yee, Long-range surface plasmons for high-resolution surface plasmon resonance sensors, Sensors Actuators B 74 (2001) 145–151, http://dx.doi.org/10.1016/s0925-4005(00)00724-3.
[39] C. Vernoux, Y. Chen, L. Markey, C. Spârchez, J. Arocas, T. Felder, M. Neitz, L. Brusberg, J.-C. Weeber, S. Bozhevolnyi, A. Dereux, Flexible long-range surface plasmon polariton single-mode waveguide for optical interconnects, Opt. Mater. Express 8 (2018) 469–484, http://dx.doi.org/10.1364/OME.8.000469.
[40] J.-Y. Jing, Q. Wang, W.-M. Zhao, B.-T. Wang, Long-range surface plasmon resonance and its sensing applications: A review, Opt. Lasers Eng. 112 (2019) 103–118, http://dx.doi.org/10.1016/j.optlaseng.2018.09.013.
[41] E. Kretschmann, H. Raether, Notizen: Zur plasmaresonanzemission im festen körper, Z. Naturforschung A 23 (4) (1968) 615–617, http://dx.doi.org/10.1515/zna-1968-0424.
[42] T. Lohner, B. Kalas, P. Petrik, Z. Zolnai, M. Serényi, G. Sáfrán, Refractive index variation of magnetron-sputtered a-$Si_{1-x}Ge_x$ by "one-sample concept" combinatory, Appl. Sci. 8 (5) (2018) 826.
[43] B. Kalas, Z. Zolnai, G. Sáfrán, M. Serényi, E. Agocs, T. Lohner, A. Németh, N.Q. Khánh, M. Fried, P. Petrik, Micro-combinatorial sampling of the optical properties of hydrogenated amorphous Si_xGe_{1-x} for the entire range of compositions towards a database for optoelectronics, Sci. Rep. 10 1 (2020) 19266.
[44] D.W. Lynch, W. Hunter, An introduction to the data for several metals, in: E.D. PALIK (Ed.), Handbook of Optical Constants of Solids, Academic Press, Boston, 1998, p. 341, http://dx.doi.org/10.1016/B978-0-08-055630-7.50018-3, URL: http://www.sciencedirect.com/science/article/pii/B9780080556307500183.
[45] O. Blazquez, J. Lopez-Vidrier, S. Hernandez, J. Montserrat, B. Garrido, Electro-optical properties of non-stoichiometric silicon nitride films for photovoltaic applications, Energy Procedia 44 (2014) 145–150, http://dx.doi.org/10.1016/j.egypro.2013.12.021.
[46] B.-H. Liao, C.-N. Hsiao, Improving optical properties of silicon nitride films to be applied in the middle infrared optics by a combined high-power impulse/unbalanced magnetron sputtering deposition technique, Appl. Opt. 53 (4) (2014) A377–A382, http://dx.doi.org/10.1364/AO.53.00A377.
[47] N. Mudgal, A. Saharia, K. Choure, A. Agarwal, G. Singh, Sensitivity enhancement with anti-reflection coating of silicon nitride (si3n4) layer in silver-based surface plasmon resonance (SPR) sensor for sensing of DNA hybridization, Appl. Phys. A 126 (2020) http://dx.doi.org/10.1007/s00339-020-04126-9.
[48] B. Kalas, J. Nador, E. Agocs, A. Saftics, S. Kurunczi, M. Fried, P. Petrik, Protein adsorption monitored by plasmon-enhanced semi-cylindrical kretschmann ellipsometry, Appl. Surf. Sci. (2017) S0169433217310802, http://dx.doi.org/10.1016/j.apsusc.2017.04.064.
[49] A.S. Lambert, S.N. Valiulis, A.S. Malinick, I. Tanabe, Q. Cheng, Plasmonic biosensing with aluminum thin films under the kretschmann configuration, Anal. Chem. 92 (13) (2020) 8654–8659, http://dx.doi.org/10.1021/acs.analchem.0c01631, arXiv:https://doi.org/10.1021/acs.analchem.0c01631, PMID: 32525300.
[50] D. Gérard, S.K. Gray, Aluminium plasmonics, J. Phys. D: Appl. Phys. 48 (18) (2014) 184001, http://dx.doi.org/10.1088/0022-3727/48/18/184001.
[51] K. Hinrichs, K.-J. Eichhorn, Ellipsometry of Functional Organic Surfaces and Films, second ed., in: Springer Series in Surface Sciences, vol. 52, Springer International Publishing, 2018.
[52] R.M.A. Azzam, N.M. Bashara, Ellipsometry and Polarized Light, North-Holland, 1977.
[53] H. Arwin, M. Poksinski, K. Johansen, Total internal reflection ellipsometry: Principles and applications, Appl. Opt. 43 (2004) 3028–3036, http://dx.doi.org/10.1364/AO.43.003028.
[54] J. Nador, B. Kalas, A. Saftics, E. Agocs, P. Kozma, L. Korosi, I. Szekacs, M. Fried, R. Horvath, P. Petrik, Plasmon-enhanced two-channel in situ kretschmann ellipsometry of protein adsorption , cellular adhesion and polyelectrolyte deposition on titania nanostructures, Opt. Express 24 (2016) 4812–4823.
[55] B. Kalas, K. Ferencz, A. Saftics, Z. Czigany, M. Fried, P. Petrik, Bloch surface waves biosensing in the ultraviolet wavelength range – bragg structure design for investigating protein adsorption by in situ kretschmann-raether ellipsometry, Appl. Surf. Sci. 536 (2021) 147869.
[56] S. Cheon, K. Kihm, H.G. Kim, G. Lim, J. Park, J. Lee, How to reliably determine the complex refractive index (RI) of graphene by using two independent measurement constraints, Sci. Rep. 4 (2014) 6364, http://dx.doi.org/10.1038/srep06364.
[57] A.D. Rakić, A.B. Djurišić, J.M. Elazar, M.L. Majewski, Optical properties of metallic films for vertical-cavity optoelectronic devices, Appl. Opt. 37 (22) (1998) 5271–5283, http://dx.doi.org/10.1364/AO.37.005271.
[58] T.-W. Lee, S. Gray, Subwavelength light bending by metal slit structures, Opt. Express 13 (2005) 9652–9659, http://dx.doi.org/10.1364/OPEX.13.009652.
[59] T.E. Tiwald, D.W. Thompson, J.A. Woollam, W. Paulson, R. Hance, Application of IR variable angle spectroscopic ellipsometry to the determination of free carrier concentration depth profiles, Thin Solid Films 313–314 (1998) 661–666.
[60] C.C. Kim, J.W. Garland, H. Abad, P.M. Raccah, Modeling the optical dielectric function of semiconductors: Extension of the critical-point parabolic-band approximation, Phys. Rev. B 45 (1992) 11749–11767, http://dx.doi.org/10.1103/PhysRevB.45.11749, URL: https://link.aps.org/doi/10.1103/PhysRevB.45.11749.
[61] D. De Sousa Meneses, G. Gruener, M. Malki, P. Echegut, Causal voigt profile for modeling reflectivity spectra of glasses, J. Non-Crystalline Solids 351 (2005) 0–129, http://dx.doi.org/10.1016/j.jnoncrysol.2004.09.028.
[62] E.A. Irene, M. Losurdo, K. Hingerl, Ellipsometry at the Nanoscale, first ed., Springer-Verlag Berlin Heidelberg, 2013.
[63] J. Moré, The Levenberg-Marquardt algorithm: Implementation and theory, in: Proceedings of the 1977 Dundee Conference on Numerical Analysis, Vol. 630, 1978, pp. 630–668.
[64] K.S.B.D. Silva, V.J. Keast, A. Gentle, M.B. Cortie, Optical properties and oxidation ofα-phase Ag–Al thin films, Nanotechnology 28 (9) (2017) 095202, http://dx.doi.org/10.1088/1361-6528/aa5782.
[65] H. Ehrenreich, H.R. Philipp, Optical properties of Ag and Cu, Phys. Rev. 128 (1962) 1622–1629, http://dx.doi.org/10.1103/PhysRev.128.1622.
[66] G. Pribil, B. Johs, N. Ianno, Dielectric function of thin metal films by combined in situ transmission ellipsometry and intensity measurements, Thin Solid Films s 455–456 (2004) 443–449, http://dx.doi.org/10.1016/j.tsf.2003.11.243.
[67] J. Gong, R. Dai, W. Zhongping, Z. Zhang, Thickness dispersion of surface plasmon of Ag nano-thin films: Determination by ellipsometry iterated with transmittance method, Sci. Rep. 5 (2015) 9279, http://dx.doi.org/10.1038/srep09279.
[68] R. Todorov, V. Katrova, P. Knotek, E. Cernoskova, M. Vlcek, Microstructure and ellipsometric modeling of the optical properties of very thin silver films for application in plasmonics, Thin Solid Films 628 (2017) 22, http://dx.doi.org/10.1016/j.tsf.2017.03.009.
[69] V.P. Drachev, U.K. Chettiar, A.V. Kildishev, H.-K. Yuan, W. Cai, V.M. Shalaev, The ag dielectric function in plasmonic metamaterials, Opt. Express 16 (2) (2008) 1186–1195, http://dx.doi.org/10.1364/OE.16.001186, URL: http://opg.optica.org/oe/abstract.cfm?URI=oe-16-2-1186.
[70] V.S.a. Wenshan Cai, Optical Metamaterials: Fundamentals and Applications, first ed., Springer-Verlag New York, 2010.
[71] U. Kreibig, Electronic properties of small silver particles: The optical constants and their temperature dependence, J. Phys. F: Metal Phys. 4 (2001) 999, http://dx.doi.org/10.1088/0305-4608/4/7/007.
[72] S. Van Gils, T. Dimogerontakis, G. Buytaert, E. Stijns, H. Terryn, P. Skeldon, G.E. Thompson, M.R. Alexander, Optical properties of magnetron-sputtered and rolled aluminum, J. Appl. Phys. 98 (8) (2005) 083505, http://dx.doi.org/10.1063/1.2085315, arXiv:https://doi.org/10.1063/1.2085315.
[73] S. Xilian, R. Hong, H. Hou, Z. Fan, J. Shao, Thickness dependence of structure and optical properties of silver films deposited by magnetron sputtering, Thin Solid Films 515 (2007) 6962–6966, http://dx.doi.org/10.1016/j.tsf.2007.02.017.
[74] Z. Ming, L. Yao-Peng, Z. Sheng, L. Ding-Quan, Optical properties and surface morphology of thin silver films deposited by thermal evaporation, Chin. Phys. Lett. 32 (2015) http://dx.doi.org/10.1088/0256-307X/32/7/077802.
[75] F. Mao, M. Taher, O. Kryshtal, A. Kruk, A. Czyrska-Filemonowicz, M. Ottosson, A.M. Andersson, U. Wiklund, U. Jansson, Combinatorial study of gradient Ag–Al thin films: Microstructure, phase formation, mechanical and electrical properties, ACS Appl. Mater. Interfaces 8 (44) (2016) 30635–30643, http://dx.doi.org/10.1021/acsami.6b10659, arXiv:https://doi.org/10.1021/acsami.6b10659, PMID: 27750408.
[76] M.D. Arnold, M.G. Blaber, Optical performance and metallic absorption in nanoplasmonic systems, Opt. Express 17 (5) (2009) 3835–3847, http://dx.doi.org/10.1364/OE.17.003835.
[77] G.B. Irani, T. Huen, F. Wooten, Optical properties of Ag and *ensurematha*-phase Ag-Al alloys, Phys. Rev. B 3 (1971) 2385–2390, http://dx.doi.org/10.1103/PhysRevB.3.2385, URL: https://link.aps.org/doi/10.1103/PhysRevB.3.2385.